Quantum Finite-Size Effects in Graphene Plasmons

Sukosin Thongrattanasiri, Alejandro Manjavacas, and F. Javier García de Abajo[†,*]

IQFR-CSIC, Serrano 119, 28006 Madrid, Spain. [†]Present address: Currently on sabbatical at Optoelectronics Research Centre, University of Southampton, Southampton SO17 1BJ, U.K.

ABSTRACT

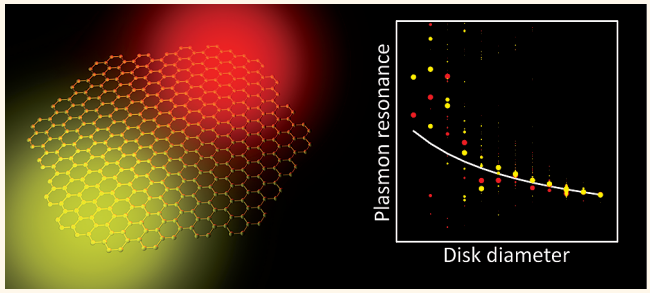

Graphene plasmons are emerging as an alternative solution to noble metal plasmons, adding the advantages of tunability *via* electrostatic doping and long lifetimes. These excitations have been so far described using classical electrodynamics, with the carbon layer represented by a local conductivity. However, the question remains, how accurately is such a classical description representing graphene? What is the minimum size for which nonlocal and quantum finite-size effects can be ignored in the plasmons of small graphene structures? Here, we provide a clear answer to these questions by performing first-principles calculations of the optical response of doped nanostructured graphene obtained from a tight-binding model for the electronic structure and the random-phase approximation for the dielectric response. The resulting plasmon energies are in good agreement with classical local electromagnetic theory down to ~10 nm sizes, below which plasmons split into several resonances that emphasize the molecular character of the carbon structures and the quantum nature of their optical excitations. Additionally, finite-size effects produce substantial plasmon broadening compared to homogeneous graphene up to sizes well above 20 nm in nanodisks and 10 nm in nanoribbons. The atomic structure of edge terminations is shown to be critical, with zigzag edges contributing to plasmon broadening significantly more than armchair edges. This study demonstrates the ability of graphene nanostructures to host well-defined plasmons down to sizes below 10 nm, and it delineates a roadmap for understanding their main characteristics, including the role of finite size and nonlocality, thus providing a solid background for the emerging field of graphene nanoplasmonics.

KEYWORDS: plasmonics · graphene plasmons · nanophotonics · tight-binding · RPA response · graphene nanodisks · nanoribbons

The collective excitations of conduction electrons in nanostructured metals known as plasmons are currently finding application in areas as diverse as ultrasensitive biosensing,[1−3] cancer therapy,[4,5] photodetection,[6] and improved photovoltaics,[7,8] out of which commercial devices are either available or expected to be released in the short term. Additionally, plasmons are being investigated for potential use in optical signal processing,[9] improved nonlinear response,[10,11] and quantum information devices.[12,13] These fields are fueled by the ability of plasmons (i) to confine electromagnetic energy down to truly nanometer scales, well below the wavelength scale imposed by the diffraction limit, and (ii) to consequently enhance the light intensity relative to externally supplied illumination.[14] However, as powerful as plasmons may seem, further exploitation of these excitations is being hampered by their limited lifetimes, typically of a few tens of optical cycles in confined configurations (*e.g.*, $\sim 10^{-13}$ s within the near-infrared). Additionally, plasmons are difficult to control without producing structural changes in the materials in which they are trapped.

In this context, the high degree of confinement and long lifetimes of plasmons in graphene compared to conventional metal plasmons[15] have stimulated intense experimental and theoretical efforts to study these collective excitations, partly triggered by the prospect of applications to metamaterials,[16,17] photodetection,[18,19] and quantum optics.[20] Besides its high degree of crystallinity compared to noble metals, graphene offers the advantage of being easily tunable *via* electrostatic gating, whereby a net density of electrons or holes is created in the carbon sheet to screen the perpendicular dc electric field produced by a nearby electrode, typically placed in a backgate configuration. This provides a convenient way to tune the Fermi energy up to >1 eV[21,22] and to electrostatically control the frequency and even the mere existence of plasmon states. The electrostatic tunability of graphene plasmons has been recently demonstrated in measurements of the terahertz light absorption by ribbons[18] and the infrared scattering strength of a tip situated near graphene.[23]

* Address correspondence to j.g.deabajo@csic.es.

Received for review December 7, 2011 and accepted January 4, 2012.

Published online January 04, 2012
10.1021/nn204780e

The optical response of graphene has been extensively investigated on theoretical grounds in homogeneous[15,20,24−26] and nanopatterned[17,19,20,27,28] structures, although most of the reported work relies on a classical electromagnetic description of the carbon sheet, which is represented by a local, frequency-dependent conductivity. A first-principles analysis including nonlocal effects has only been performed for extended graphene[15,24,25,29] and for plasmon energies in narrow (<1.5 nm) armchair ribbons.[30] The latter exhibit plasmons even when they are undoped, in contrast to zigzag ribbons,[30] thus indicating that carbon edge terminations play an important role in the band structure and the optical response of nanostructured graphene. Such a dramatic dependence on carbon edges is accompanied by opening of electron band gaps (∼20 meV for a width of 25 nm) and formation of localized edge states in zigzag ribbons.[30−34] Although these effects are expected to be small in samples with characteristic dimensions above 100 nm, a comprehensive study in truly nanometer-sized structures is still missing.

In this article, we present first-principles calculations of the optical response of graphene nanodisks and nanoribbons. We describe doped graphene using a tight-binding model for the electronic structure[35,36] and the random-phase approximation (RPA)[37] for the dielectric response. The resulting plasmon energies are predicted to follow quite closely those obtained from classical electrodynamics, except for sizes below ∼10 nm, for which the molecular character of the carbon structures shows up by splitting the plasmon features into an increasing number of resonances as the size is reduced. In contrast, the plasmon lifetime displays a slower convergence toward classical theory and remains well below the relaxation time of homogeneous graphene even in structures larger than 20 nm. Our results demonstrate that doped graphene is capable of sustaining plasmons down to sub-10 nm structures, whose understanding requires going beyond classical local electrodynamics.

RESULTS AND DISCUSSION

First-Principles Description of Graphene Plasmons. At low energies below ∼1 eV, the optical response of carbon allotropes is dominated by excitations of the π valence band, formed by electrons residing in the carbon 2p orbitals oriented perpendicularly with respect to the local carbon bonds and populated on average with one electron per carbon site (*i.e.*, this band is half filled due to spin degeneracy). The σ band lies deeper in energy and only contributes with a nearly uniform background polarization. Excited states are formed when π electrons hop between neighboring sites, and thus, it is natural to study the π band within a tight-binding model, in which one-electron states are linear combinations of carbon 2p orbitals (one per site).[35] A tight-binding Hamiltonian is then defined as explained in the Methods section. Despite its simplicity, the tight-binding model provides a reliable description of the electronic structure,[36] particularly when used inside the RPA susceptibility (see below), which is an integrated quantity that should be rather insensitive to corrections affecting individual electron levels due to many-body interations[38,39] and edge effects.[40] As a first step in our calculation, we diagonalize this Hamiltonian for patterned graphene and find its single-electron states. For finite structures formed by N atoms (*e.g.*, nanodisks), this leads to a set of N doubly spin-degenerate states. In neutral graphene, only half of them are occupied, but in doped graphene configurations, they are filled up to a Fermi energy (E_F) relative to undoped carbons sheets.

The structures under discussion are small compared to the light wavelength, and consequently, they are accurately described within the electrostatic limit, in which the charge density ρ_l induced on each carbon site l can be expressed in terms of the self-consistent potential $\phi_{l'}$ acting at all sites l' as

$$\rho_l = \sum_{l'} \chi^0_{ll'} \phi_{l'} \qquad (1)$$

where $\chi^0_{ll'}$ is the noninteracting susceptibility. Furthermore, we obtain χ^0 using the RPA,[37] in which only electron−hole pair excitations are considered. The susceptibility is then constructed from the expansion coefficients a_{jl} of the tight-binding states $\sum_l a_{jl}|l\rangle$, where j is a state label and l runs over carbon sites. More precisely[37]

$$\chi^0_{ll'}(\omega) = \frac{2e^2}{\hbar} \sum_{jj'} (f_{j'} - f_j) \frac{a_{jl} a^*_{jl'} a^*_{j'l} a_{j'l'}}{\omega - (\varepsilon_j - \varepsilon_{j'}) + i/2\tau} \qquad (2)$$

where ω is the light frequency, $\hbar\varepsilon_j$ is the energy of state j and $f_j = \{\exp[\hbar\varepsilon_j - E_F)/k_BT] + 1\}^{-1}$ is its occupation at temperature T (we set $T = 300$ K throughout this work), τ is an intrinsic relaxation time,[41] and the factor of 2 before the sum stems from spin degeneracy. A direct evaluation of χ^0 for a carbon cluster formed by N atoms (*e.g.*, $N \sim 12\,000$ for 20 nm disks) constitutes a *tour de force* that requires summing $\sim N^4$ terms, so instead, we employ an alternative procedure based upon the use of the fast Fourier transform (FFT), which reduces the task to $\sim N^3$ operations, as explained in the Methods section. Incidentally, the orthogonality of the electron states directly implies $\sum_l \chi^0_{ll'} = 0$, and this in turn guarantees the vanishing of the net induced charge $\sum_l \rho_l = 0$ (see eq 1). Now, the total potential is the sum of the external potential ϕ^{ext} and the potential produced by the induced charges:

$$\phi_l = \phi^{ext}_l + \sum_{l'} v_{ll'} \rho_{l'} \qquad (3)$$

where $v_{ll'}$ is the Coulomb interaction produced on the p orbital at site l by a unit charge with the distribution of the p orbital at site l'. This interaction is roughly $1/r$ for $l \neq l'$, whereas $v_{ll} = 0.58$ atomic units (au). Nonetheless, we calculate $v_{ll'}$ rigorously using the probability distribution

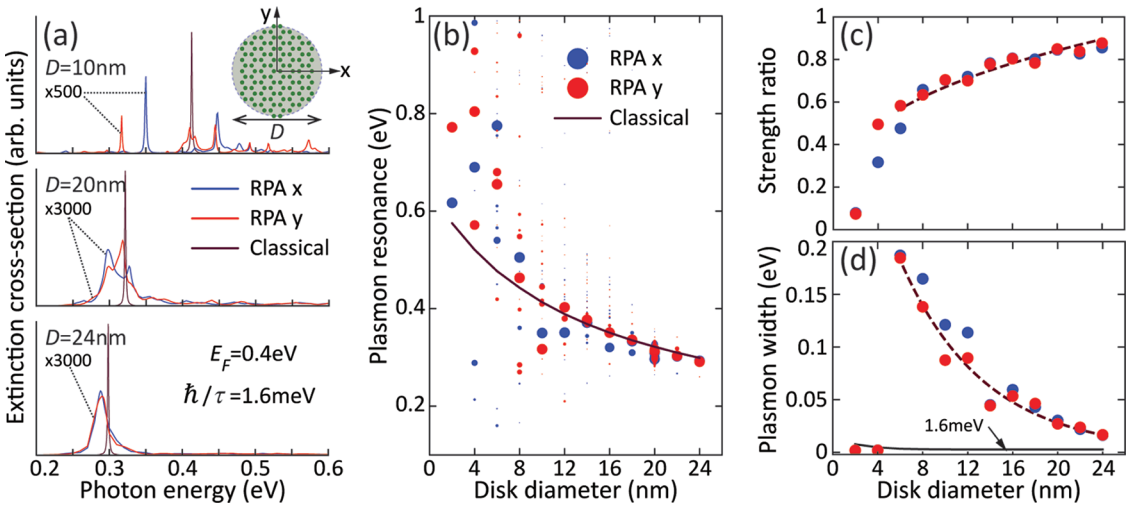

Figure 1. Plasmons in graphene nanodisks. (a) Extinction cross section calculated in the RPA for self-standing graphene disks of different size and for incidence perpendicular to the disks with polarizations along the *x* or *y* directions (see inset), compared with classical electromagnetic theory. The main features in the plot correspond to induced parallel dipoles. (b) Spectral features in the extinction spectra (symbols) compared with the classical electromagnetic dipole plasmon energy as a function of disk size. The symbol sizes are scaled with the strength of the spectral peaks. (c) Ratio of integrated area in the spectra calculated within the RPA to the classical plasmon peak area. (d) Plasmon half-area width in our RPA calculations (symbols) and in the classical theory (lower curve, which roughly coincides with the input width $\hbar\tau^{-1}$ = 1.6 meV). Dashed curves in (c) and (d) are guides to the eye. The Fermi energy is E_F = 0.4 eV in all cases.

associated with carbon 2p orbitals taken from tabulated atomic data.[42] We self-consistently solve eqs 1 and 3 to find ρ_l and then compute the absorption cross section

$$\sigma^{abs} = 4\pi(\omega/c)\mathrm{Im}\{\alpha(\omega)\}$$

from the polarizability α, which is in turn given by the dipole induced upon illumination with a uniform electric field $\mathbf{E}^{ext}$ (*i.e.*, $\phi_l^{ext} = -x_l E^{ext}$) as

$$\alpha(\omega) = (1/E^{ext})\sum_l x_l\rho_l$$

where x_l are the projections of the atomic coordinates along the external field direction.

Finite-Size and Nonlocal Effects in Graphene Nanodisks. We show in Figure 1a several examples of extinction spectra calculated for graphene nanodisks of different size and a common doping level (E_F = 0.4 eV). A first striking observation is the presence of multiple peaks in the smallest disk under consideration (diameter D = 10 nm). Rather than a proper clearly defined plasmon, the spectra for both orientations of the incident light polarization relative to the carbon lattice exhibit several narrow peaks, the width of which is roughly equal to the intrinsic width $\hbar\tau^{-1}$ introduced through eq 2. For larger structures (D = 20 and 24 nm), these peaks evolve toward a single prominent peak of larger width, rather independent of the orientation of the incident polarization. A similar trend toward a single plasmon peak is observed when increasing the intrinsic width (see Figure S6 in the Supporting Information). When compared with a classical calculation of the extinction (black curves), we see that this is in fact the dipolar plasmon sustained by these structures. The classical calculation is based upon a description of the graphene in terms of a frequency-dependent local surface conductivity, which is then used to match the electromagnetic boundary conditions imposed by Maxwell's equations in the presence of the nanodisks (see Methods). Remarkably, the classically calculated plasmon exhibits a narrow width $\sim\hbar\tau^{-1}$, in contrast to the much broader plasmon features predicted by our first-principles RPA calculations.

Figure 1b presents a summary of nanodisk extinction spectra obtained as a function of disk diameter for polarizations either along *x* or *y* (see inset in Figure 1a). The actual spectra are given in the Supporting Information (Figure S8). For each value of the diameter, this plot contains several symbols indicating the different peaks that show up in the spectra. The size of each symbol is roughly proportional to the strength of the corresponding peak. We observe a clear trend of convergence of spectral features toward a single plasmon band as the diameter increases. Actually, convergence toward the plasmon energy predicted by the classical model is nearly achieved for diameters above ~20 nm. For smaller sizes, the strength of the plasmon is generally situated at larger energies (*i.e.*, it is blue-shifted) compared to the classical calculation.

In order to quantify the plasmon width for small diameters, given the complex structure of the spectra, we introduce the half-area width, which we define as the accumulated width of a spectral region centered around the average plasmon energy and containing half of the integrated area under the spectrum (in particular, the half-area width is equal to the fwhm for single Lorentzian peaks). In practice, we define a

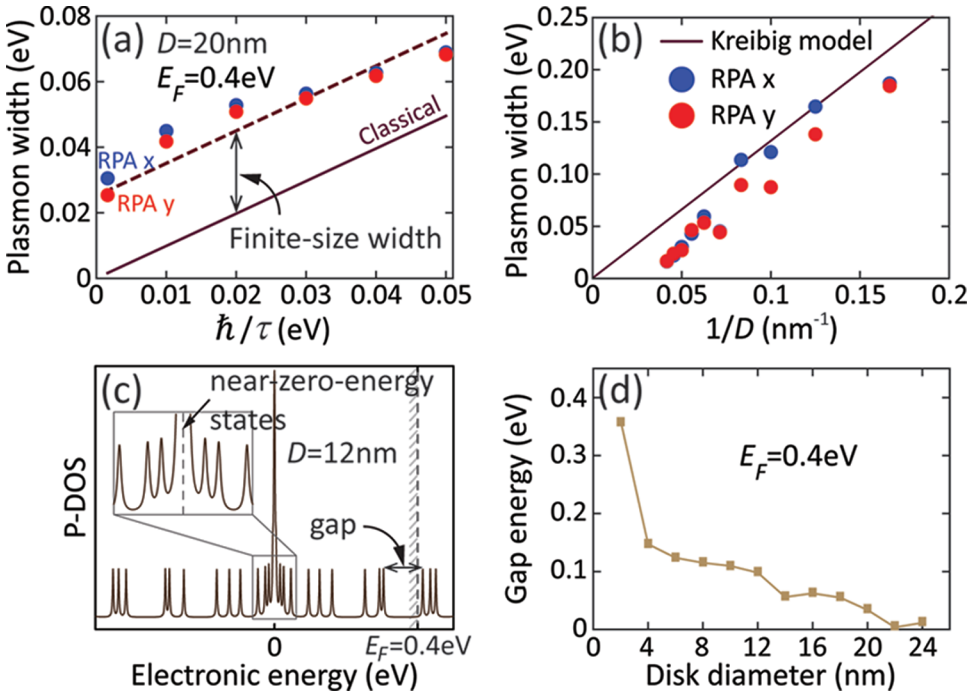

Figure 2. Finite-size and nonlocal effects in the plasmons of graphene nanodisks. (a) Evolution of the half-area dipole plasmon width as a function of input intrinsic width $\hbar\tau^{-1}$. A nearly constant difference between these two is found and denoted finite-size width. (b) Variation of the finite-size width with disk diameter D, showing a roughly linear dependence with $1/D$. The straight line corresponds to a plasmon width given by $2\hbar v_F/D$. (c) Pseudodensity of states (P-DOS) in a 12 nm disk, showing a gap near the Fermi energy E_F = 0.4 eV and near-zero-energy states. (d) Gap energy dependence on disk size.

spectral window in the 0−1 eV range for this purpose. A trend of convergence toward the classical result ($\sim\hbar\tau^{-1}$), similar to what happened with the plasmon energy, is observed for the plasmon width, although this is still well above the intrinsic damping $\hbar\tau^{-1}$ even for a relatively large diameter D = 24 nm (Figure 1d). (Incidentally, small disks of 2 nm in diameter only display one peak within the spectral window under consideration (see Supporting Information, Figure S8), the width of which roughly corresponds to the intrinsic damping. Larger disks contain several peaks, and this explains the sudden jump in plasmon width.) Likewise, the ratio of plasmon areas calculated from the RPA and from the classical model (Figure 1c, with the areas integrated over the noted spectral window) is slowly converging toward 1 with increasing diameter. It should be noted that the finite-size effects under discussion occur even for plasmon energies well below E_F (large diameters in Figure 1), and therefore, their origin is different from Landau damping taking place in homogeneous graphene when the plasmon band overlaps the electron−hole excitation region at plasmon energies roughly above the Fermi energy.

The additional finite-size width of the plasmon with respect to the intrinsic width $\hbar\tau^{-1}$ seems to be well preserved over a large range of τ (Figure 2a), thus indicating that it is consistently produced by finite-size and edge effects. It rapidly decreases with increasing disk diameter (Figure 2b), although it is still taking considerable values well above $\hbar\tau^{-1}$ for D = 24 nm. This behavior can be ultimately understood by noticing the finite spectral separation between different individual excitations in small structures (see Figure 1a and Figure S8 in the Supporting Information), which, even after incorporating the interaction between excited electron−hole pairs in a self-consistent fashion through the RPA, continue to be separated by a considerable distance in photon energy. For finite relaxation time τ, these peaks coalesce into a single broader plasmon feature (see Figure S6 in the Supporting Information), thus transforming the energy distance between individual excitations into an effective broadening of the plasmon as a whole.

At this point, it is useful to examine the distribution of electronic energies. For example, a disk with D = 12 nm and E_F = 0.4 eV (Figure 2c) exhibits a characteristic electronic gap near the Fermi level that defines a minimum excitation energy and, therefore, also an optical gap. Moreover, it displays a pileup of electron states around zero energy, essentially localized near zigzag edges of the graphene nanodisk (see Figures S3 and S4 in the Supporting Information for more details). The complex interplay between electronic states *via* their mutual orthogonality enters this picture by producing more broadening (*i.e.*, larger energy separation between the constituent individual excitations noted above) when edge states are present (see also a related discussion for ribbons in next section). One might naively think that near-zero-energy edge states only contribute to broadening for plasmon energies

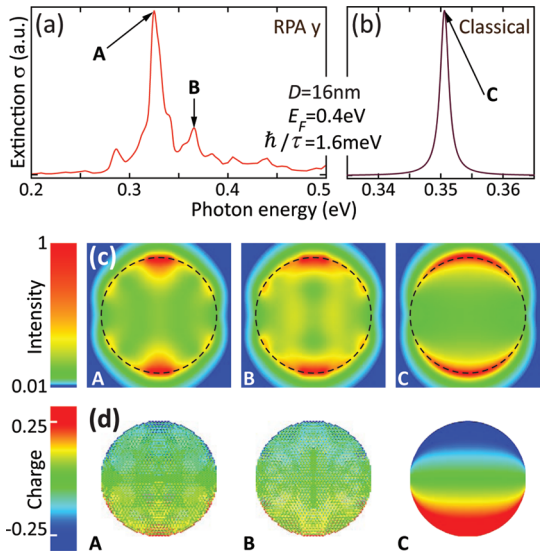

Figure 3. Fine structure in the plasmon features. (a,b) Extinction spectrum for a disk with physical parameters as shown by text insets, calculated within the RPA (a) and from a classical model (b). Light is incident normal to the disk with the electric field along the *y* direction. (c) Normalized electric field intensity (log scale) at a distance of 0.5 nm above the disk for features A and B of the RPA spectrum, compared to the classical calculation (C). The intensity enhancement relative to the incident field is 810, 64, and 2.7×10^5 in A–C, respectively. (d) Normalized charge-density amplitude (linear scale saturated outside [−0.25,0.25]) for the same features as in (c).

exceeding the Fermi energy (see Figure 2c), but this is at odds with the smooth dependence of the plasmon width on disk size around the point where the plasmon energy is crossing E_F (*i.e.*, $D \approx 12$ nm; see Figure 1b,d). A possible mechanism of decoherence is related to the distortion of the electronic wave functions near zigzag edges, which is needed in order to fulfill the orthogonality of every electron state with respect to edge states. This distortion can potentially provide extra momentum needed to produce additional electron–hole pair transitions that couple to the plasmon, in contrast to the stringent momentum conservation conditions in homogeneous graphene. The electronic gap can also influence the plasmon width by limiting the number of available electron–hole transitions for a given plasmon energy. In this respect, it is interesting to note that the gap exhibits a similar trend as the finite-size width, with a strong decrease toward zero as the disk diameter increases.

The plasmon width shows a nearly linear dependence on $1/D$ (Figure 2b), similar to that of metallic nanoparticles.[43,44] This is phenomenologically understood from Kreibig's model,[43] which associates the extra broadening with the time spanned between electron (or hole) edge collisions. The relevant electrons are moving at a speed close to the Fermi velocity v_F, and the increase in the plasmon decoherence rate for nanoparticles of diameter D is $\sim 2v_F/D$.[43] The straight line in Figure 2b corresponds to $2\hbar v_F/D$, in excellent agreement with the RPA width. This supports the interpretation of the nanodisk plasmon width as originating in quantum confinement and finite-size effects, similar to what happens in metal nanoparticles. However, in contrast to nanoparticles, small disks of size below ~10 nm exhibit multiple excitations that emphasize the molecular character of these structures (see Supporting Information, Figure S8), possibly due to the low number of involved graphene electrons compared to metal nanoparticles of similar diameter. The role of edge states discussed above also introduces a clear difference with respect to nanoparticles.

The spectral structure of the plasmon is expected to be complex, as it results from accumulation of multiple peaks toward a single plasmon energy as the disk diameter increases. This is clearly illustrated in Figure 3, where a disk of size $D = 16$ nm is analyzed. The plasmon is not yet fully consisting of a single peak for the values of D and $\hbar\tau^{-1} = 1.6$ meV under consideration (Figure 3a). We show the near-field and the induced charge associated with two of the spectral features within the plasmon region, and we find very different spatial behavior (cf. A and B in Figure 3c,d), particularly when compared to the classical model (C). Additionally, the field enhancement obtained from the RPA is considerably smaller than that predicted by classical theory (see caption of Figure 3), in agreement with recent calculations for metallic dimers.[45] This information is important for assessing the strength of the interaction between this structure and additional elements such as molecules for potential use in biosensing or to achieve strong light–matter interaction.[20]

Understanding Edge Effects in Nanoribbon Plasmons. An extension of the formalism presented above allows us to simulate graphene nanoribbons (see Methods). In particular, we consider ribbons with either zigzag or armchair edges exposed to a uniform electric field directed across the ribbon width, from which we calculate the absorption cross section under normal incidence conditions. The main results are summarized in Figure 4, which presents the evolution of the plasmon energy and the plasmon width for different edge terminations. Like in the nanodisks studied above, nanoribbon plasmons are dipolar and thus couple efficiently to external light. In contrast to disks, nanoribbons exhibit a single plasmon feature down to very small widths, presumably due to the fact that electron–hole transitions are summed over a continuum of electron parallel wave vectors along the ribbon direction (*i.e.*, the electronic spectrum is continuous in ribbons, but it is discrete in nanodisks). The plasmon energies obtained from first-principles calculations (Figure 4b, symbols) nicely converge toward the classical result for sizes above ~10 nm and show a small blue shift at small ribbon widths. The plasmon width also converges toward the intrinsic value determined by τ (Figure 4c), but this convergence is

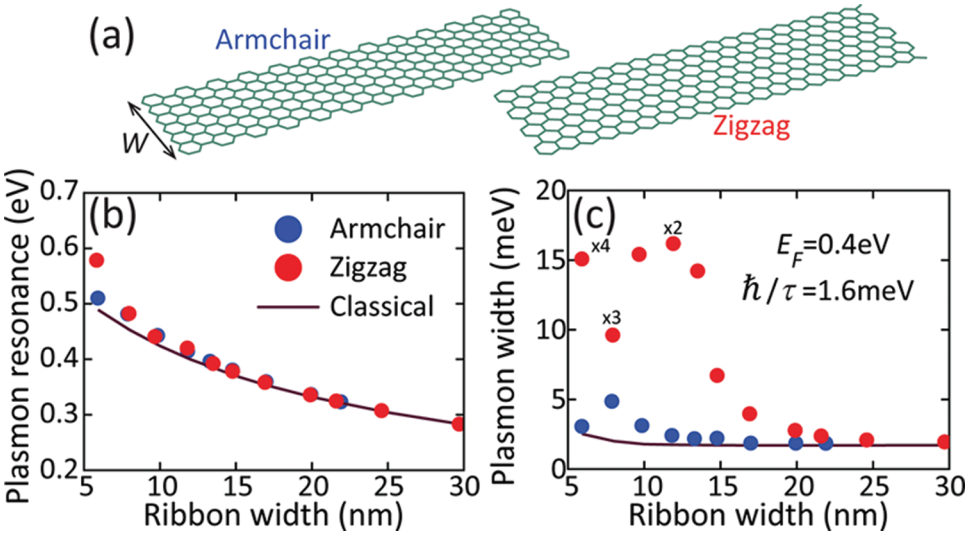

Figure 4. Plasmons in nanoribbons. (a) We consider nanoribbons with armchair and zigzag edges. The relative alignment between both edges is clearly shown in the figure. (b) Variation of the plasmon energy with ribbon width, calculated in the RPA (symbols) and from a classical electromagnetic description (curve). (c) Plasmon half-area width as a function of ribbon width.

remarkably faster in armchair ribbons. In contrast, zigzag ribbons host electron states confined to the edges,[31] which seem to be responsible for the additional plasmon broadening.

Comparing ribbons and disks of similar size (width = diameter), the plasmon width in nanodisks is almost 1 order of magnitude larger than in zigzag ribbons (cf. Figure 1d and Figure 4c). This suggests that plasmon broadening in nanodisks and nanoribbons is due to different physical mechanisms. Quantum confinement can produce plasmon broadening because the plasmon finds new electron−hole pair excitations into which it can decay compared to homogeneous graphene; the finite size of the electron (hole) wave functions translates into extra momentum to fulfill energy-momentum conservation. This mechanism should be more efficient in nanodisks than in nanoribbons because disks have larger perimeter-to-area ratio. The inhomogeneous edges and edge-state distributions in nanodisks also contribute in a similar manner to broaden the plasmon, as explained above. These mechanisms are compatible with the large calculated broadening of nanodisk plasmons, exhibiting a nearly linear dependence on $1/D$ (Figure 2b). In contrast, the width of nanoribbon plasmons displays a more complicated dependence on the inverse ribbon width $1/W$ (see Supporting Information, Figure S10). We expect quantum confinement to be less effective in nanoribbons because the electron states are free to move along the spatial direction parallel to them. Edge states in zigzag ribbons are thus the likely origin of additional plasmon broadening in these structures, although their effect is diminished with respect to nanodisks because ribbons have uniform edges. These conclusions are further supported by the fact that armchair ribbons, in which edge states are not present, display a much smaller plasmon broadening, comparable in magnitude to the classical calculation.

Edge states emerge with near-zero energy,[31] so they contribute to the plasmon width for plasmon energies above E_F *via* excitation to unoccupied conduction states. This is what we observe in Figure 4: the plasmon energy exceeds the Fermi energy when the ribbon width drops below ~12 nm (Figure 4b), and the plasmon width rises enormously in narrower zigzag ribbons (Figure 4c). However, the width of zigzag ribbon plasmons is significantly larger than that of armchair ribbon plasmons up to a ribbon width of ≈20 nm, thus pointing to an additional mechanism other than direct excitation of edge states. A possible explanation is provided by the distinct band structures of armchair and zigzag ribbons, which allow transitions between states of opposite wave vector along the ribbon direction only in zigzag ribbons,[30] thus increasing the number of electron−hole decay channels available to the plasmons.

We have recently shown that for the ribbon widths W under consideration (≪ light wavelength) an electrostatic scaling law applies to the classically calculated plasmon frequency, namely[28]

$$\eta = \frac{\mathrm{Im}\{\sigma(\omega_p)\}}{\omega_p W} \qquad (4)$$

where σ is the graphene surface conductivity and η is just a constant that only depends on the direction of light incidence and mode polarization. Under normal incidence conditions, the dipole plasmon frequency is obtained by setting $\eta = 0.0675$. Then, using the local RPA model for σ, as described in the Methods section, the solution of eq 4 yields a plasmon frequency that cannot be distinguished from the solid curve of

Figure 4b (full electrodynamic calculations) on the scale of the plot. Additionally, in the Drude model, the electrostatic scaling law predicts that the plasmon width equals the intrinsic width $\hbar\tau^{-1}$,[28] in good agreement with the solid curve of Figure 4c, except for ribbons of small width, <10 nm, for which the plasmon energy lies above E_F, thus being broadened by Landau damping, not accounted for by Drude. It is remarkable that this simple analytical law is in quantitative agreement with the RPA calculations here presented for the plasmon energy in ribbons wider than 10 nm and also for the plasmon width in armchair ribbons wider then ~10 nm and in zigzag ribbons wider than ~20 nm.

CONCLUSIONS

We have performed first-principles calculations of the optical response of doped graphene nanodisks and nanoribbons within the RPA using a tight-binding model for the electronic states. The plasmon width and frequency are dramatically influenced by nonlocal and quantum finite-size effects, compared to a classical electromagnetic description reported elsewhere.[20] Similar to what happens in small metallic nanoparticles,[43−47] plasmon blue shifts are clearly observable due to these effects up to nanodisk diameters and ribbon widths above ~10 nm. Plasmon broadening is also significant up to sizes above ~25 nm compared to the plasmon width in homogeneous graphene. We attribute these effects to both the finite size of the structures and the presence of electronic edge states. In particular, localized electron states are supported by zigzag edges[31] (see Supporting Information, Figures S3 and S4), which lead to extra plasmon broadening in ribbons with that kind of termination as compared to ribbons of similar size but with armchair edges instead. For small structures below ~20 nm, nanodisk plasmons display considerable fine structure that is clearly resolvable even when considering a conservative intrinsic broadening, thus emphasizing the molecular character of nanostructured graphene. This is in contrast to nanoribbons, which exhibit a single plasmon feature within the range of ribbon widths under consideration (5−30 nm). Actually, nanoribbons and nanoparticles share in common a large number of electronic states and optical transitions compared to nanodisks, which lead to a single plasmon feature rather than molecule-like modes at small sizes.

Plasmons in nanoribbons wider than 10 nm have been shown to rapidly converge in energy to the results predicted by classical electrodynamics, although the plasmon width is significantly affected by finite-size and edge effects in ribbons of widths below ~10 nm for armchair terminations and below ~20 nm in zigzag ribbons. Nanodisks contain a combination of these types of edge terminations, and thus, they are affected by edge states, as well. Actually, the ratio of edge perimeter to graphene area is larger in nanodisks, which is consistent with the fact that plasmon blue shifts and broadenings occur in these structures up to large diameters compared to the ribbon widths. It must be noted that such small graphene structures have been recently synthesized,[48] therefore making the experimental verification of our work feasible in the short term, although it is still technically challenging to combine the required nanofabrication tools with good control over graphene doping and infrared optical measurements.

It is useful to realize that the number of electrons needed to dope a $D = 20$ nm graphene nanodisk up to a Fermi energy $E_F = 0.4$ eV is only $\approx (E_F D/2\hbar v_F)^2 \approx 37$, where we use the electron density in doped homogeneous graphene ($n = E_F^2/(\pi\hbar^2 v_F^2)$) for this estimate. Adding or removing one extra electron thus requires an attainable change of ≈5 meV in E_F, which results in a shift by ≈2 meV in plasmon energy, according to the electrostatic scaling law[28] ($\omega_p^2 D/E_F$ = constant), although actual values might be influenced by the finiteness of the electronic gap. These numbers point to the unprecedented possibility of inducing observable plasmon shifts by electrically injecting one single electron to the graphene structure. Careful analysis of finite-size effects is required to analyze this phenomenon, which can find application to optical switching with ultrasmall amounts of electric energy.

In practical terms, nanodisk doping presents a technical challenge because of the damaging effects that conventional metallic leads can have on the optical response of the structure. Decorating the disks with bridges made of a transparent, conductive material can be a solution, whereas chemical doping is another option, which can be useful for achieving optical sensing of chemical changes in a fluid surrounding the graphene. Aternatively, local doping in a small graphene region of an extended flake can be driven by a nearby charged metal tip, so that the resulting structure mimics a nanodisk of diameter comparable to the tip−graphene separation. This configuration should allow plasmons to be confined in the doped region, possibly exhibiting increased plasmon lifetimes due to the absence of damaging edge states.

In summary, a classical electromagnetic treatment is a reasonable approximation only for graphene ribbons and disks with characteristic dimensions of at least several tens of nanometers, whereas a proper quantum description of the electronic states and their collective excitations as presented here is needed for smaller sizes. Our work is thus serving two purposes: (i) it provides a solid justification for the use of classical theory in large structures; and (ii) it presents a landscape for plasmons in smaller structures, which can find potential application to nanophotonic devices

(*e.g.*, in plasmon−molecule interactions, ultrasensitive optical detection through SERS or SEIRA, and the noted variation of plasmon energy by adding or removing one single electron to/from a graphene nanoisland), but require careful treatment of nonlocal and finite-size effects.

METHODS

Tight-Binding Model. In the tight-binding approach, the one-electron states j in the π band are constructed as linear combinations of carbon 2p orbitals $\sum_l a_{jl}|l\rangle$, where l runs over carbon sites. Incidentally, we disregard spin−orbit interactions, so that electron spin enters the RPA response just through an overall factor of 2 in the noninteracting susceptibility χ^0 (see eq 2). We assume orthogonality between site states, $\langle l|l'\rangle = \delta_{ll'}$. The only nonzero elements of the tight-binding Hamiltonian H involve nearest neighbors l and l', for which $\langle l|H|l'\rangle = -t$, where the hopping energy t is a fitting parameter. In homogeneous graphene, this model predicts a band structure characterized by two inequivalent so-called Dirac cones, crossing the Fermi level at two inequivalent K corner points of the hexagonal first Brillouin zone with an energy dependence $\approx \pm\hbar v_F|k|$,[35,49] where k is the electron wave vector relative to the corresponding Dirac point, $v_F \approx 3ta_0/2\hbar$ is the Fermi velocity, and $a_0 = 1.421$ Å is the C−C bond distance. The Dirac cone has been traced through photoemission measurements,[50] from which fine corrections to the band structure have been resolved, although we expect them to be washed out by summing over electron−hole pairs in χ^0. The measured Fermi velocity $v_F \approx 10^6$ m/s leads to a hopping parameter $t \approx 3.1$ eV, which is close to the actual value that we use here ($t \approx 2.8$ eV), deduced from both STM measurements of graphene nanoislands[48] and fits to *ab initio* calculations.[36] Incidentally, we neglect next-nearest-neighbor hopping, which is believed to contribute to H with terms ~0.1 eV.[51] Furthermore, we are treating carbon edges with the same hopping parameter and perfect hexagonal structure as atoms in homogeneous graphene, while a more proper description leads to reconstruction and modified electronic wave functions,[52] but summation over states in χ^0 should minimize this type of effect. In this respect, first-principles calculations beyond the tight-binding model have been reported for nanoribbons,[53,54] from which no significant corrections are expected to emerge in the optical response.

Evaluation of the RPA Susceptibility in N^3 Time Using the Fast Fourier Transform. Direct summation of eq 2 involves $\sim N^4$ operations. This task becomes currently unaffordable for the size of the structures considered in this work. Instead, we evaluate χ^0 in N^3 time by writing[55,56]

$$\chi^0_{ll'}(\omega) = \frac{2e^2}{\hbar}\int \frac{S_{ll'}(\omega')\mathrm{d}\omega'}{\omega - \omega' + i/2\tau} \tag{5}$$

where

$$\begin{aligned} S_{ll'}(\omega) &= \sum_{jj'}(f_{j'} - f_j)a_{jl}a^*_{jl'}a^*_{j'l}a_{j'l'}\delta[\omega - (\varepsilon_j - \varepsilon_{j'})] \\ &= \int d\omega'[F_{ll'}(\omega')G^*_{ll'}(\omega' - \omega) - G_{ll'}(\omega')F^*_{ll'}(\omega' - \omega)] \end{aligned} \tag{6}$$

is a spectral function and

$$\begin{bmatrix} F_{ll'}(\omega) \\ G_{ll'}(\omega) \end{bmatrix} = \sum_j a_{jl}a^*_{jl'}\delta(\omega - \varepsilon_j)\begin{bmatrix} 1 - f_j \\ f_j \end{bmatrix} \tag{7}$$

are auxiliary functions, the evaluation of which takes a time proportional to N^3 (see below). The integral of eq 6 is then carried out using the FFT. Details on the convergence of this method are provided in the Supporting Information (Figure S5). Incidentally, according to eqs 1 and 3, the self-consistent potential acting on the carbon atoms reduces to $\phi = (1 - v\cdot\chi^0)^{-1}\cdot\phi^{\mathrm{ext}}$, where the dot indicates matrix multiplication and the atomic-site label l is used as the matrix index. The matrix inversion needed to evaluate ϕ also takes a time $\sim N^3$.

The electron energies are limited to a finite range $\hbar|\varepsilon_j| < \hbar\omega_{\max}$, and therefore, we only need to compute the auxiliary functions $F_{ll'}(\omega)$ and $G_{ll'}(\omega)$ for ω within that range, over which we define a finite grid of N_ω frequencies ω_n. In order to facilitate the convolution discussed below, we take equally spaced frequencies, and N_ω is chosen to be a power of 2. We evaluate the auxiliary functions by splitting the weight of the δ functions in eq 7 into neighboring frequencies, so that each term j contributes to $F_{ll'}(\omega_n)$ as[55] $a_{jl}a^*_{jl'}(1 - f_j)(\varepsilon_j - \omega_n)/(\omega_{n+1} - \omega_n)$ and to $F_{ll'}(\omega_{n+1})$ as $a_{jl}a^*_{jl'}(1 - f_j)(\omega_{n+1} - \varepsilon_j)/(\omega_{n+1} - \omega_n)$, and likewise for G, with ε_j lying between ω_n and ω_{n+1}. This procedure has to be repeated over the N^2 combinations of sites l and l' for each of the N states j, so that it takes a time $\sim N^3$, with independence of the number of frequencies N_ω.

We evaluate the convolution of eq 6 using the FFT in a time roughly proportional to $N \log_2 N_\omega$ for each combination of l and l', thus preserving the approximate N^3 time scaling of the overall computation. This yields $S_{ll'}(\omega_n)$ over a frequency grid spanning the range $|\omega_n| < 2\omega_{\max}$. The FFT is actually carried out using the FFTW package.[57]

Finally, the integral of eq 5 is calculated from S by performing the frequency integral over each element of the ω grid:

$$\chi^0_{ll'}(\omega) \approx \sum_n W_n S_{ll'}(\omega_n)$$

where the weights

$$\begin{aligned} W_n = \frac{4e^2}{\hbar}\Bigg[&\int_{\omega_n}^{\omega_{n+1}} \frac{\omega' d\omega'}{(\omega + i/2\tau)^2 - \omega'^2}\left(\frac{\omega_{n+1} - \omega'}{\omega_{n+1} - \omega_n}\right) \\ &+ \int_{\omega_{n-1}}^{\omega_n} \frac{\omega' d\omega'}{(\omega + i/2\tau)^2 - \omega'^2}\left(\frac{\omega' - \omega_{n-1}}{\omega_n - \omega_{n-1}}\right)\Bigg] \end{aligned} \tag{8}$$

are analytically computed once and for all the first time that they are needed.

RPA for Nanoribbons. We consider nanoribbons of period b along their direction of translational symmetry, containing N carbon atoms in the unit cell. We describe electronic states of ribbons with zigzag and armchair edges within the tight-binding model, which faithfully follows the ribbon electronic structures previously reported in the literature.[31] More precisely, we use Bloch's theorem[58] to construct a complete set of electron eigenstates labeled by both the carbon site index l within the first unit cell and the Bloch wave vector k spanning the first Brillouin zone ($|kb| < \pi$). The eigenstate amplitudes thus become $a_{jl,k}e^{ikbn}$, where the integer n runs over unit cells. It is convenient to decompose the externally applied field in terms of its Fourier components along the ribbon direction z, on which they depend as $\phi^{\mathrm{ext}}_{l,q}e^{iqz}$. After some algebra, we find that the induced charge density and the potential depend on n through a factor e^{iqbn}; the total potential reads

$$\phi_{l,q} = \phi^{\mathrm{ext}}_{l,q} + \sum_{l'} v_{ll',q}\rho_{l',q}$$

where

$$v_{ll',q} = \sum_n v_{l0,l'n}e^{iqbn}$$

involves a sum of the Coulomb interaction $v_{l0,l'n}$ between atoms l and l' separated by n unit cells (charge neutrality, leading to

$\Sigma_{l'}\chi^0_{ll'} = 0$, allows us to subtract $1/|nb|$, from $n \neq 0$ terms in this sum to accelerate its convergence); the induced density becomes $\rho_{l,q} = \Sigma_{l'}\chi^0_{ll',q}\phi_{l',q}$; and the noninteracting RPA susceptibility appropriate for the 1D translational symmetry reads

$$\chi^0_{ll',q}(\omega) = \sum_n \chi_{l0,l'n} e^{iqbn} \approx \frac{2e^2}{\hbar}\frac{b}{2\pi}\int_{-\pi/b}^{\pi/b} dk \sum_{jj'} (f_{j',k-q} - f_{j,k}) \frac{a_{jl,k}a^*_{j'l,k-q}a^*_{j'l',k-q}a_{jl',k}}{\omega - (\varepsilon_{j,k} - \varepsilon_{j',k-q}) + i/2\tau}$$

where we have approximated $qb \ll 1$. We compute $\chi^0_{ll',q}$ by performing the k integral using N_k equally spaced points. In practice, we use $N_k \sim 10^4$ to achieve convergence in the spectra for $\hbar\tau^{-1} \sim 2$ meV. We apply this formalism to a uniform electric field E^{ext} oriented along the ribbon width (*i.e.*, an external potential $-x_l E^{ext}$ with $q = 0$, where x_l is the coordinate of atom l along the graphene direction normal to z). Finally, the absorption cross section reduces to

$$\sigma = \frac{4\pi\omega L}{c}\sum_l x_l \mathrm{Im}\left\{\frac{\rho_{l,q=0}}{E^{ext}}\right\}$$

where L is the ribbon length.

Intrinsic Relaxation Time. In practice, τ in eq 2 represents an intrinsic relaxation time produced by inelastic electron−electron, electron−phonon, and electron−impurity scattering. Actually, electron−phonon coupling plays a leading role at plasmon energies above the in-plane optical phonon energy ~0.2 eV.[15,34] A first-principles treatment of the relaxation time must involve many-body interactions, whose computation is outside the scope of the present work and becomes extremely challenging even for homogeneous graphene.[38,39] Here, unless otherwise stated, we take the empirical value $\tau = 10^{-12}E_F$ in seconds, where E_F is expressed in eV, as estimated from a measured dc mobility of 10 000 cm^2/(V·s).[15,59,60] This renders τ large compared to the relaxation produced by finite-size and edge effects in the nanostructures under discussion, and therefore, the conclusions of our work are rather independent of the exact choice of τ.

Classical Electromagnetic Calculations. We compare our RPA results with classical electromagnetic theory throughout this paper. Classical theory is computed here by rigorously solving the Maxwell equations using the boundary element method (BEM)[20,61] for nanodisks and nanoribbons. In the BEM, graphene is modeled as a thin film of edges rounded by semicircular profiles and characterized by a dielectric function $1 + 4\pi i\sigma/\omega t$, where t is the film thickness and $\sigma(\omega)$ is the frequency-dependent surface conductivity. We use $t = 0.1$ nm, which is well converged with respect to the $t \to 0$ limit (see Supporting Information, Figures S12 and S13). Most importantly, we take $\sigma(\omega)$ from the local limit of the random-phase approximation for extended graphene (*i.e.*, for zero parallel wave vector), which is available in analytical form in the literature[24,25] and reproduced in the Supporting Information for convenience. By construction, this classical approach must exactly converge to our RPA calculations in the limit of large disk radius or ribbon width for vanishing parallel wave vector. However, dramatic deviations between the RPA and the classical local theory are reported in this work for disks (ribbons) of finite radius (width), which are shown to decrease with increasing disk (ribbon) size beyond a few tens of nanometers.

Acknowledgment. We thank F. Guinea, F.H.L. Koppens, and D. Sánchez-Portal for helpful and enjoyable discussions. This work has been supported in part by the Spanish MICINN (MAT2010-14885 and Consolider NanoLight.es) and the European Commission (FP7-ICT-2009-4-248909-LIMA and FP7-ICT-2009-4-248855-N4E). A.M. acknowledges financial support through FPU from the Spanish ME.

Supporting Information Available: We provide additional information on the construction of carbon atom clusters for tight-binding calculations, one-electron states, electron edge states, convergence of the FFT method for the evaluation of χ^0, dependence of calculated absorption spectra on the relaxation time τ, sensitivity of those spectra to edge terminations, cluster size dependence of absorption, plasmon-peak structure, the local RPA conductivity of homogeneous graphene, and convergence of electromagnetic calculations with graphene thickness. This material is available free of charge *via* the Internet at http://pubs.acs.org.

REFERENCES AND NOTES

1. Xu, H.; Bjerneld, E. J.; Käll, M.; Börjesson, L. Spectroscopy of Single Hemoglobin Molecules by Surface Enhanced Raman Scattering. *Phys. Rev. Lett.* **1999**, *83*, 4357–4360.
2. Talley, C. E.; Jackson, J. B.; Oubre, C.; Grady, N. K.; Hollars, C. W.; Lane, S. M.; Huser, T. R.; Nordlander, P.; Halas, N. J. Surface-Enhanced Raman Scattering from Individual Au Nanoparticles and Nanoparticle Dimer Substrates. *Nano Lett.* **2005**, *5*, 1569–1574.
3. Álvarez-Puebla, R. A.; Liz-Marzán, L. M.; Garca de Abajo, F. J. Light Concentration at the Nanometer Scale. *J. Phys. Chem. Lett.* **2010**, *1*, 2428–2434.
4. O'Neal, D. P.; Hirsch, L. R.; Halas, N. J.; Payne, J. D.; West, J. L. Photo-Thermal Tumor Ablation in Mice Using Near Infrared-Absorbing Nanoparticles. *Cancer Lett.* **2004**, *209*, 171–176.
5. Loo, C.; Lowery, A.; Halas, N. J.; West, J. L.; Drezek, R. Inmunotargeted Nanoshells for Integrated Cancer Imaging and Therapy. *Nano Lett.* **2005**, *5*, 709–711.
6. Knight, M. W.; Sobhani, H.; Nordlander, P.; Halas, N. J. Photodetection with Active Optical Antennas. *Science* **2011**, *332*, 702–704.
7. Catchpole, K. R.; Polman, A. Plasmonic Solar Cells. *Opt. Express* **2008**, *16*, 21793–21800.
8. Atwater, H. A.; Polman, A. Plasmonics for Improved Photovoltaic Devices. *Nat. Mater.* **2010**, *9*, 205–213.
9. Zia, R.; Schuller, J. A.; Chandran, A.; Brongersma, M. L. Plasmonics: The Next Chip-Scale Technology. *Mater. Today* **2006**, *9*, 20–27.
10. Danckwerts, M.; Novotny, L. Optical Frequency Mixing at Coupled Gold Nanoparticles. *Phys. Rev. Lett.* **2007**, *98*, 026104.
11. Harutyunyan, H.; Palomba, S.; Renger, J.; Quidant, R.; Novotny, L. Nonlinear Dark-Field Microscopy. *Nano Lett.* **2010**, *10*, 5076–5079.
12. Chang, D. E.; Sorensen, A. S.; Demler, E. A.; Lukin, M. D. A Single-Photon Transistor Using Nanoscale Surface Plasmons. *Nat. Phys.* **2007**, *3*, 807–812.
13. Manjavacas, A.; García de Abajo, F. J.; Nordlander, P. N. Quantum Plexcitonics: Strongly Interacting Plasmons and Excitons. *Nano Lett.* **2011**, *11*, 2318–2323.
14. Novotny, L.; Hecht, B. *Principles of Nano-Optics*; Cambridge University Press: New York, 2006.
15. Jablan, M.; Buljan, H.; Soljačić, M. Plasmonics in Graphene at Infrared Frequencies. *Phys. Rev. B* **2009**, *80*, 245435.
16. Papasimakis, N.; Luo, Z.; Shen, Z. X.; De Angelis, F.; Di Fabrizio, E.; Nikolaenko, A. E.; Zheludev, N. I. Graphene in a Photonic Metamaterial. *Opt. Express* **2010**, *18*, 8353–8359.
17. Vakil, A.; Engheta, N. Transformation Optics Using Graphene. *Science* **2011**, *332*, 1291–1294.
18. Ju, L.; Geng, B.; Horng, J.; Girit, C.; Martin, M.; Hao, Z.; Bechtel, H. A.; Liang, X.; Zettl, A.; Shen, Y. R.; *et al.* Graphene Plasmonics for Tunable Terahertz Metamaterials. *Nat. Nanotechnol.* **2011**, *6*, 630–634.
19. Thongrattanasiri, S.; Koppens, F. H. L.; García de Abajo, F. J. Total Light Absorption in Graphene; arXiv:1106.4460v1.
20. Koppens, F. H. L.; Chang, D. E.; García de Abajo, F. J. Graphene Plasmonics: A Platform for Strong Light−Matter Interactions. *Nano Lett.* **2011**, *11*, 3370–3377.
21. Efetov, D. K.; Kim, P. Controlling Electron−Phonon Interactions in Graphene at Ultrahigh Carrier Densities. *Phys. Rev. Lett.* **2010**, *105*, 256805.
22. Chen, C. F.; Park, C. H.; Boudouris, B. W.; Horng, J.; Geng, B.; Girit, C.; Zettl, A.; Crommie, M. F.; Segalman, R. A.; Louie, S. G.; *et al.* Controlling Inelastic Light Scattering Quantum Pathways in Graphene. *Nature* **2011**, *471*, 617–620.
23. Fei, Z.; Andreev, G. O.; Bao, W.; Zhang, L. M.; McLeod, A. S.; Wang, C.; Stewart, M. K.; Zhao, Z.; Dominguez, G.; Thiemens, M.; *et al.* Infrared Nanoscopy of Dirac Plasmons at the Graphene−SiO_2 Interface. *Nano Lett.* **2011**, *11*, 4701–4705.

24. Wunsch, B.; Stauber, T.; Sols, F.; Guinea, F. Dynamical Polarization of Graphene at Finite Doping. *New J. Phys.* **2006**, *8*, 318.
25. Hwang, E. H.; Das Sarma, S. Dielectric Function, Screening, and Plasmons in Two-Dimensional Graphene. *Phys. Rev. B* **2007**, *75*, 205418.
26. Nikitin, A. Y.; Guinea, F.; García-Vidal, F. J.; Martn-Moreno, L. Fields Radiated by a Nanoemitter in a Graphene Sheet. *Phys. Rev. B* **2011**, *84*, 195446.
27. Nikitin, A. Y.; Guinea, F.; Garca-Vidal, F. J.; Martn-Moreno, L. Edge and Waveguide Terahertz Surface Plasmon Modes in Graphene Microribbons. *Phys. Rev. B* **2011**, *84*, 161407(R).
28. Christensen, J.; Manjavacas, A.; Thongrattanasiri, S.; Koppens, F. H. L.; García de Abajo, F. J. Graphene Plasmon Waveguiding and Hybridization in Individual and Paired Nanoribbons. *ACS Nano* **2011**, DOI: 10.1021/nn2037626.
29. Yan, J.; Thygesen, K. S.; Jacobsen, K. W. Nonlocal Screening of Plasmons in Graphene by Semiconducting and Metallic Substrates: First-Principles Calculations. *Phys. Rev. Lett.* **2011**, *106*, 146803.
30. Brey, L.; Fertig, H. A. Elementary Electronic Excitations in Graphene Nanoribbons. *Phys. Rev. B* **2007**, *75*, 125434.
31. Brey, L.; Fertig, H. A. Electronic States of Graphene Nanoribbons Studied with the Dirac Equation. *Phys. Rev. B* **2006**, *73*, 235411.
32. Son, Y. W.; Cohen, M. L.; Louie, S. G. Energy Gaps in Graphene Nanoribbons. *Phys. Rev. Lett.* **2006**, *97*, 216803.
33. Han, M. Y.; Özyilmaz, B.; Zhang, Y.; Kim, P. Energy Band-Gap Engineering of Graphene Nanoribbon. *Phys. Rev. Lett.* **2007**, *98*, 206805.
34. Beams, R.; Cancado, L. G.; Novotny, L. Low Temperature Raman Study of the Electron Coherence Length near Graphene Edges. *Nano Lett.* **2011**, *11*, 1177–1181.
35. Wallace, P. R. The Band Theory of Graphite. *Phys. Rev.* **1947**, *71*, 622–634.
36. Reich, S.; Maultzsch, J.; Thomsen, C.; Ordejón, P. Tight-Binding Description of Graphene. *Phys. Rev. B* **2002**, *66*, 035412.
37. Pines, D.; Nozières, P. *The Theory of Quantum Liquids*; W.A. Benjamin, Inc.: New York, 1966.
38. Trevisanutto, P. E.; Giorgetti, C.; Reining, L.; Ladisa, M.; Olevano, V. *Ab Initio* GW Many-Body Effects in Graphene. *Phys. Rev. Lett.* **2008**, *101*, 226405.
39. Park, C. H.; Giustino, F.; Spataru, C. D.; Cohen, M. L.; Louie, S. G. First-Principles Study of Electron Linewidths in Graphene. *Phys. Rev. Lett.* **2009**, *102*, 076803.
40. Wimmer, M.; Akhmerov, A. R.; Guinea, F. Robustness of Edge States in Graphene Quantum Dots. *Phys. Rev. B* **2010**, *82*, 045409.
41. The RPA response depends on ω through $(\omega + i/2\tau)^2 \approx \omega(\omega + i/\tau)$ (see eq 8). We introduce the factor of 1/2 in $\omega + i/2\tau$ (*e.g.*, in eq 2) in order to mimic the $\omega(\omega + i/\tau)$ dependence of the Drude model, which is consistent with electron-number conservation, as demonstrated in Mermin, N. D. Lindhard Dielectric Function in the Relaxation-Time Approximation. *Phys. Rev. B* **1970**, *1*, 2362–2363. This approximation is justified by the large values of τ under consideration.
42. Clementi, E.; Roetti, C. Roothaan-Hartree-Fock Atomic Wavefunctions. *At. Data Nucl. Data Tables* **1974**, *14*, 177–478.
43. Kreibig, U.; Genzel, L. Optical Absorption of Small Metallic Particles. *Surf. Sci.* **1985**, *156*, 678–700.
44. Halperin, W. P. Quantum Size Effects in Metal Particles. *Rev. Mod. Phys.* **1986**, *58*, 533–606.
45. Zuloaga, J.; Prodan, E.; Nordlander, P. Quantum Description of the Plasmon Resonances of a Nanoparticle Dimer. *Nano Lett.* **2009**, *9*, 887–891.
46. Kreibig, U.; Vollmer, M. *Optical Properties of Metal Clusters*; Springer-Verlag: Berlin, 1995.
47. García de Abajo, F. J. Nonlocal Effects in the Plasmons of Strongly Interacting Nanoparticles, Dimers, and Waveguides. *J. Phys. Chem. C* **2008**, *112*, 17983–17987.
48. Phark, S.; Borme, J.; Vanegas, A. L.; Corbetta, M.; Sander, D.; Kirschner, J. Direct Observation of Electron Confinement in Epitaxial Graphene Nanoislands. *ACS Nano* **2011**, *5*, 8162–8166.
49. Castro Neto, A. H.; Guinea, F.; Peres, N. M. R.; Novoselov, K. S.; Geim, A. K. The Electronic Properties of Graphene. *Rev. Mod. Phys.* **2009**, *81*, 109–162.
50. Bostwick, A.; Ohta, T.; Seyller, T.; Horn, K.; Rotenberg, E. Quasiparticle Dynamics in Graphene. *Nat. Photonics* **2007**, *3*, 36–40.
51. Deacon, R. S.; Chuang, K. C.; Nicholas, R. J.; Novoselov, K. S.; Geim, A. K. Cyclotron Resonance Study of the Electron and Hole Velocity in Graphene Monolayers. *Phys. Rev. B* **2007**, *76*, 081406(R).
52. van Ostaay, J. A. M.; Akhmerov, A. R.; Beenakker, C. W. J.; Wimmer, M. Dirac Boundary Condition at the Reconstructed Zigzag Edge of Graphene. *Phys. Rev. B* **2011**, *84*, 195434.
53. Prezzi, D.; Varsano, D.; Ruini, A.; Marini, A.; Molinari, E. Optical Properties of Graphene Nanoribbons: The Role of Many-Body Effects. *Phys. Rev. B* **2008**, *77*, 041404(R).
54. Agapito, L. A.; Cheng, H. P. *Ab Initio* Calculation of a Graphene-Ribbon-Based Molecular Switch. *J. Phys. Chem. C* **2007**, *111*, 14266–14273.
55. Shishkin, M.; Kresse, G. Implementation and Performance of the Frequency-Dependent GW Method within the PAW Framework. *Phys. Rev. B* **2006**, *74*, 035101.
56. Foerster, D.; Koval, P.; Sánchez-Portal, D. An $O(N^3)$ Implementation of Hedin's *GW* Approximation for Molecules. *J. Chem. Phys.* **2011**, *135*, 074105.
57. Frigo, M.; Johnson, S. G. The Design and Implementation of FFTW3. *Proc. IEEE* **2005**, *93*, 216–231.
58. Ashcroft, N. W.; Mermin, N. D. *Solid State Physics*; Harcourt College Publishers: New York, 1976.
59. Novoselov, K. S.; Geim, A. K.; Morozov, S. V.; Jiang, D.; Zhang, Y.; Dubonos, S. V.; Grigorieva, I. V.; Firsov, A. A. Electric Field Effect in Atomically Thin Carbon Films. *Science* **2004**, *306*, 666–669.
60. Novoselov, K. S.; Geim, A. K.; Morozov, S. V.; Jiang, D.; Katsnelson, M. I.; Grigorieva, I. V.; Dubonos, S. V.; Firsov, A. A. Two-Dimensional Gas of Massless Dirac Fermions in Graphene. *Nature* **2005**, *438*, 197–200.
61. García de Abajo, F. J.; Howie, A. Retarded Field Calculation of Electron Energy Loss in Inhomogeneous Dielectrics. *Phys. Rev. B* **2002**, *65*, 115418.